

A nonlinear approach for the three-dimensional polyhedron scaled boundary finite element method and its verification using Koyna gravity dam

Kai Chen^{a,b}, Degao Zou^{a,b,*}, Xianjing Kong^{a,b}

^a The State Key Laboratory of Coastal and Offshore Engineering, Dalian University of Technology, Dalian, Liaoning 116024, China

^b School of Hydraulic Engineering, Dalian University of Technology, Dalian, Liaoning 116024, China

ARTICLE INFO

Keywords:

Scaled boundary finite element
Three-dimensional
Polyhedron
Nonlinear
Plastic-damage model

ABSTRACT

Since it was presented, the scaled boundary finite element method (SBFEM) has been shown to be versatile and has been widely applied in structural numerical simulations. However, as it is analytical in the radial direction, nonlinearity inside elements cannot be considered, limiting its application in elastic fields. In this paper, a nonlinear approach for the three-dimensional polyhedron scaled boundary finite element (NPSBFEM3D) is proposed for elasto-plastic analysis to remove this restriction. In NPSBFEM3D, conforming shape functions are constructed using the semi-analytical solution derived from elastic surface elements, while the integrations are accomplished using internal Gauss points in the radial direction instead of integrating on the boundary surface elements. Eventually, the proposed approach can be as conveniently used in elasto-plastic analysis as FEM. This method permits an arbitrary number of faces, which offers a promising adaptive capacity for modelling. Three simulations are conducted to verify the robustness of the presented method.

1. Introduction

The finite element method (FEM) and the boundary element method (BEM) are undisputedly powerful computational techniques for numerical simulation. In the FEM, all computational dimensions need to be discretized. Usually, a polynomial shape function is used to interpolate the displacement inside an element. The solution can be derived from the equilibrium equation after obtaining the stiffness and mass matrices using a standard integration rule; this method offers versatility and convenience. As it only requires discretization of the boundary, one spatial dimension can be reduced in the BEM, reducing the pretreatment and unknowns. However, a fundamental solution is required, which is relatively complicated and requires special integration techniques [1].

The scaled boundary finite element method (SBFEM) was developed by Wolf and Song in the mid-1990s [2]. The entire boundary of each element must be directly visible from the scaling centre. This method combines the advantages of the FEM and the BEM while avoiding their limitations. The discretization and assembly concepts are inherited from the FEM. However, following the BEM, discretization is only conducted on the boundary but does not require a fundamental solution, which minimizes the discretization effort and

substantially decreases the degrees of freedom (DOFs). In addition, a novel personal characteristic is exhibited: an analytical solution can be obtained in the radial direction, and a numerical solution can be obtained in the circumferential direction.

This method was initially developed to manage the unbounded problem and was called the consistent infinitesimal finite element cell method. It was later renamed SBFEM when the concept for solving the problems was better understood. The application of this method for bounded fields has been presented according to the similarity theory, and exhaustive diffusion equations are derived in the book *Finite-Element Modelling of Unbounded Media* by Wolf and Song [2]. Later, the governing partial equations were redefined using the weighted residual technique, which is consistent with the FEM. The SBFEM has been employed in various engineering fields and has received rapid recognition. Specifically, Goswami S [3], Sascha Hell [4], Saputra AA [5,6], and many others have used this method to conduct three-dimensional (3D) crack analysis. Additional researchers who used this method include Man H [7], who simulated plate bending, Liu J [8] et al., who presented solutions for a magneto-electro-elastic plate, and Gravenkamp H [9] et al., who calculated the dispersion relations for 3D elastic waveguides. Birk C [10] et al. using the modified SBFEM to model dynamic soil-structure interactions in layered soil. Combining

* Corresponding author at: The State Key Laboratory of Coastal and Offshore Engineering, Dalian University of Technology, Dalian, Liaoning 116024, China.
E-mail address: zoudegao@dlut.edu.cn (D. Zou).

the SBFEM with other methods improves the computational efficiency and broadens the application fields. Yang ZJ et al. developed an efficient method for analysing the mesoscale crack propagation of concrete [11,12]. Luo et al. modelled the particle breakage in granular media using a method that coupled the SBFEM with the discrete element method (DEM) [13]. However, this method is semi-analytical: an analytical solution can be obtained in the radial direction, and a numerical solution can be obtained in the circumferential direction. With this feature, nonlinear properties inside the elements cannot be described. Therefore, the previously mentioned SBFEM applications have so far been limited to linear elastic materials. For problems that involve material nonlinearity, a coupled approach is usually adopted.

Material nonlinearity is an inevitable problem in the numerical simulations for many engineering structures, especially for simulations of fatigue damage accumulation, structural destruction and geotechnical engineering structures, which show ubiquitous nonlinearity. To the authors' knowledge, the SBFEM has so far been developed for only simple nonlinear partial differential equations [14], the applications of which are still rare. A few researchers have performed plane nonlinear analysis by improving or coupling this method with FEM. For instance, Ooi E T [15] et al. derived the first scaled boundary polygon formulation for elasto-plastic analyses. A homotopy analysis method (HAM) was later proposed to extend SBFEM to nonlinear simulations [16]. For 3D problems, the Hilber-Hughes-Taylor- α (HHT- α) technique has been added to the coupled SBFEM-FEM approach to model the elasto-plastic soil-structure interaction [17]. A distinctive approach is developed in this paper.

Based on previous studies, this study presents a distinctive nonlinear polyhedron SBFEM, and the detail description is as follows: The non-dimensional variable ξ varies from 0 to 1 at the scaling centre and at the surface boundary. According to the Gaussian integration rule, the two planes where the radial coordinate ξ is equal to $0.5 \times (1 \pm \frac{\sqrt{3}}{3})$ are chosen in each pyramid covered by the boundary surface element. In addition, four Gauss points scaled from the isoparametric surface element are adopted in each plane. The conforming shape function is constructed with these inserted points using the semi-analytical solution derived from elastic theory. Then, the elasto-plastic constitutive matrix is computed from the plastic constitutive module. Next, the stiffness matrix, the internal load vector, and the internal stresses are calculated using Gauss integration over a polyhedron, similar to FEM. The partial polyhedron elements are generated by borrowing the octree concept. The three-dimensional polyhedron scaled boundary finite element (NPSBFEM3D) inherits the intrinsic advantages while offering additional flexibility, which is efficient for managing cross-scale mesh. This method offers promising adaptive capacity for modelling, which may provide significant potential in practical applications.

This paper is structured as follows: The basic theoretical derivation of the SBFEM is introduced in Section 2. The displacement field, the shape function of the polyhedron elements and the incremental strain and stress fields are also described in that section. Section 3 describes the scaled boundary polyhedron formulation for elasto-plastic analysis. The development platform for the proposed algorithm is introduced in Section 4. The reliability of the procedure is validated through two numerical examples in Section 5. Section 6 summarizes the major conclusions that can be drawn from this study.

2. Summary of the SBFEM

The essential theory of the SBFEM is summarized in this section. The key equations necessary for explaining the solution procedure and implementation are provided here.

2.1. Governing equations of elastic-statics

The governing equations of 3D elastic-statics are formulated in the

Cartesian coordinates \hat{x} , \hat{y} and \hat{z} . A circumflex (\wedge) is introduced to denote a point in space, as the coordinates x , y , and z are reserved for the boundary, which is discretized in a simulation. To simplify the nomenclature, the circumflex is omitted when used to indicate a direction in a subscript.

The displacements at a point in a 3D domain are denoted as shown in Eq. (2-1), and the strains ϵ are written as shown in Eq. (2-2):

$$\{u(\hat{x}, \hat{y}, \hat{z})\} = [u_x(\hat{x}, \hat{y}, \hat{z}), u_y(\hat{x}, \hat{y}, \hat{z}), u_z(\hat{x}, \hat{y}, \hat{z})]^T \quad (2-1)$$

$$\begin{aligned} \{\epsilon(\hat{x}, \hat{y}, \hat{z})\} \\ = \\ [\epsilon_x(\hat{x}, \hat{y}, \hat{z}), \epsilon_y(\hat{x}, \hat{y}, \hat{z}), \epsilon_z(\hat{x}, \hat{y}, \hat{z}), \gamma_{yz}(\hat{x}, \hat{y}, \hat{z}), \gamma_{xz}(\hat{x}, \hat{y}, \hat{z}), \gamma_{xy}(\hat{x}, \hat{y}, \hat{z})]^T \end{aligned} \quad (2-2a)$$

$$\{\epsilon(\hat{x}, \hat{y}, \hat{z})\} = [L]\{u(\hat{x}, \hat{y}, \hat{z})\} \quad (2-2b)$$

where L is the linear differential operator, which is

$$[L] = \begin{bmatrix} \frac{\partial}{\partial \hat{x}} & & & & & \\ & \frac{\partial}{\partial \hat{y}} & & & & \\ & & \frac{\partial}{\partial \hat{z}} & & & \\ & \frac{\partial}{\partial \hat{z}} & \frac{\partial}{\partial \hat{y}} & & & \\ \frac{\partial}{\partial \hat{z}} & & \frac{\partial}{\partial \hat{x}} & & & \\ \frac{\partial}{\partial \hat{y}} & \frac{\partial}{\partial \hat{x}} & & & & \end{bmatrix} \quad (2-3)$$

Then, the equilibrium in elastic-statics is formulated as shown in Eq. (2-4), and the stresses are written as shown in Eq. (2-5), using the symmetric positive definite elasticity matrix $[D]$.

$$[L]^T \{\sigma(\hat{x}, \hat{y}, \hat{z})\} = 0 \quad (2-4)$$

$$\{\sigma(\hat{x}, \hat{y}, \hat{z})\} = [D]\{\epsilon(\hat{x}, \hat{y}, \hat{z})\} \quad (2-5)$$

2.2. Scaled boundary transformation of geometry

In the SBFEM, a so-called scaling centre O is introduced in a zone from which the total boundary must be directly visible (Fig. 1(a)). As in the BEM, the discretization and assembly concepts are applied on only the boundary, which significantly minimizes the discretization processing and substantially reduces the DOFs.

Abundant documentation can be obtained on the key derivations of the SBFEM and its solution schemes in many other papers (e.g. [1,2,5,7]). Therefore, this paper outlines a 3D illustration of a bounded elastic problem to introduce some key equations for later reference. For a 3D problem, the boundary S of the problem domain V is discretized with a surface element. A typical quadrilateral surface element with four nodes on the partial boundary S^e (superscript 'e' for element) is illustrated in Fig. 2(a), and the corresponding parent element is shown

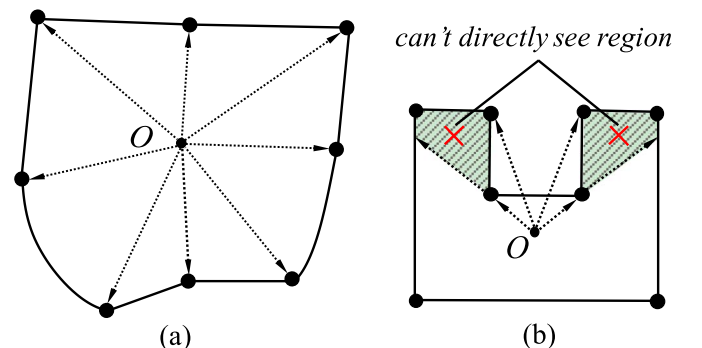


Fig. 1. Demand for scaling centre (a) Boundary is completely visible (b) Boundary is not visible completely.

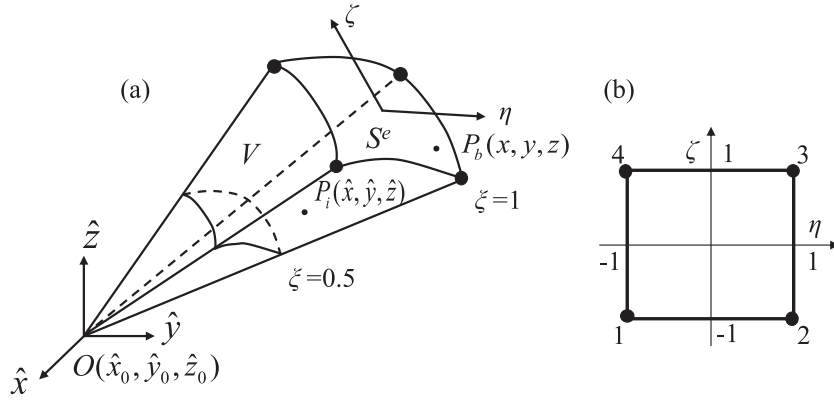


Fig. 2. 3D scaled boundary coordinates: (a) scaling centre O , dimensional radial coordinate ξ and one surface element on the boundary (b) four-node surface parent element.

in Fig. 2(b).

The scaled boundary coordinate system (ξ, η, ζ) is introduced, similar to FEM, where ξ denotes the radial coordinate and η and ζ are the circumferential coordinates. Then, the domain of the isoparametric quadrilateral element is interpolated using the shape functions $[N(\eta, \zeta)]$ formulated in the local coordinates η and ζ :

$$\begin{aligned} x(\eta, \zeta) &= [N(\eta, \zeta)]\{\mathbf{x}\} \\ y(\eta, \zeta) &= [N(\eta, \zeta)]\{\mathbf{y}\} \\ z(\eta, \zeta) &= [N(\eta, \zeta)]\{\mathbf{z}\} \end{aligned} \quad (2-6)$$

where $\{\mathbf{x}\}$, $\{\mathbf{y}\}$, $\{\mathbf{z}\}$ are the coordinate vectors of the nodes on the boundary. Thus, each point on the boundary can be fully described by the element shape functions and the local coordinate (η, ζ) in a corresponding element. The geometry of a pyramid is described by scaling the boundary with a dimensionless radial coordinate ξ that connects the scaling centre $O(\hat{x}_0, \hat{y}_0, \hat{z}_0)$ and the nodes on the boundary (Fig. 2a). At the scaling centre, ξ is equal to zero, and at the boundary, ξ is equal to one. The pyramid shows the region resulting from scaling the element on S^e . The scaled outer image of the boundary is obtained by scaling all the Cartesian coordinates of the boundary with the same scaling factor ξ .

$$\begin{aligned} \hat{x}(\xi, \eta, \zeta) &= \xi[N(\eta, \zeta)]\{\mathbf{x}\} + \hat{x}_0 \\ \hat{y}(\xi, \eta, \zeta) &= \xi[N(\eta, \zeta)]\{\mathbf{y}\} + \hat{y}_0 \\ \hat{z}(\xi, \eta, \zeta) &= \xi[N(\eta, \zeta)]\{\mathbf{z}\} + \hat{z}_0 \end{aligned} \quad (2-7)$$

(ξ, η, ζ) are the scaled boundary coordinates in a 3D domain. Changing the coordinates from $(\hat{x}, \hat{y}, \hat{z})$ to (ξ, η, ζ) is called the *scaled boundary transformation*.

A standard procedure is applied to accomplish the transformation, similar to FEM. The Jacobian matrix and determinant on the boundary are shown in Eq. (2-8).

$$[J(\eta, \zeta)] = \begin{bmatrix} x(\eta, \zeta) & y(\eta, \zeta) & z(\eta, \zeta) \\ x(\eta, \zeta)_{,\eta} & y(\eta, \zeta)_{,\eta} & z(\eta, \zeta)_{,\eta} \\ x(\eta, \zeta)_{,\zeta} & y(\eta, \zeta)_{,\zeta} & z(\eta, \zeta)_{,\zeta} \end{bmatrix} \quad (2-8a)$$

$$|J(\eta, \zeta)| = x(y_{,\eta}z_{,\zeta} - z_{,\eta}y_{,\zeta}) + y(z_{,\eta}x_{,\zeta} - x_{,\eta}z_{,\zeta}) + z(x_{,\eta}y_{,\zeta} - y_{,\eta}x_{,\zeta}) \quad (2-8b)$$

where the derivatives are evaluated as:

$$\begin{aligned} x(\eta, \zeta)_{,\eta} &= N_{,\eta}(\eta, \zeta)\{\mathbf{x}\} \\ y(\eta, \zeta)_{,\eta} &= N_{,\eta}(\eta, \zeta)\{\mathbf{y}\} \\ z(\eta, \zeta)_{,\eta} &= N_{,\eta}(\eta, \zeta)\{\mathbf{z}\} \end{aligned} \quad (2-9)$$

The linear differential operator in Eq. (2-2) is written in the (η, ζ) coordinates as:

$$[L] = \mathbf{b}_1(\eta, \zeta) \frac{\partial}{\partial \xi} + \frac{1}{\xi} \left(\mathbf{b}_2(\eta, \zeta) \frac{\partial}{\partial \eta} + \mathbf{b}_3(\eta, \zeta) \frac{\partial}{\partial \zeta} \right) \quad (2-10)$$

where $\mathbf{b}_1(\eta, \zeta)$, $\mathbf{b}_2(\eta, \zeta)$, and $\mathbf{b}_3(\eta, \zeta)$ are defined as:

$$\mathbf{b}_1(\eta, \zeta) = \frac{1}{|J|} \begin{bmatrix} y_{,\eta}z_{,\zeta} - z_{,\eta}y_{,\zeta} & 0 & 0 \\ 0 & z_{,\eta}x_{,\zeta} - x_{,\eta}z_{,\zeta} & 0 \\ 0 & 0 & x_{,\eta}y_{,\zeta} - y_{,\eta}x_{,\zeta} \\ 0 & x_{,\eta}y_{,\zeta} - y_{,\eta}x_{,\zeta} & z_{,\eta}x_{,\zeta} - x_{,\eta}z_{,\zeta} \\ x_{,\eta}y_{,\zeta} - y_{,\eta}x_{,\zeta} & 0 & y_{,\eta}z_{,\zeta} - z_{,\eta}y_{,\zeta} \\ z_{,\eta}x_{,\zeta} - x_{,\eta}z_{,\zeta} & y_{,\eta}z_{,\zeta} - z_{,\eta}y_{,\zeta} & 0 \end{bmatrix} \quad (2-11a)$$

$$\mathbf{b}_2(\eta, \zeta) = \frac{1}{|J|} \begin{bmatrix} zy_{,\zeta} - yz_{,\zeta} & 0 & 0 \\ 0 & xz_{,\zeta} - zx_{,\zeta} & 0 \\ 0 & 0 & yx_{,\zeta} - xy_{,\zeta} \\ 0 & yx_{,\zeta} - xy_{,\zeta} & xz_{,\zeta} - zx_{,\zeta} \\ yx_{,\zeta} - xy_{,\zeta} & 0 & zy_{,\zeta} - yz_{,\zeta} \\ xz_{,\zeta} - zx_{,\zeta} & zy_{,\zeta} - yz_{,\zeta} & 0 \end{bmatrix} \quad (2-11b)$$

$$\mathbf{b}_3(\eta, \zeta) = \frac{1}{|J|} \begin{bmatrix} yz_{,\eta} - zy_{,\eta} & 0 & 0 \\ 0 & zx_{,\eta} - xz_{,\eta} & 0 \\ 0 & 0 & xy_{,\eta} - yx_{,\eta} \\ 0 & xy_{,\eta} - yx_{,\eta} & zx_{,\eta} - xz_{,\eta} \\ xy_{,\eta} - yx_{,\eta} & 0 & yz_{,\eta} - zy_{,\eta} \\ zx_{,\eta} - xz_{,\eta} & yz_{,\eta} - zy_{,\eta} & 0 \end{bmatrix} \quad (2-11c)$$

2.3. Nodal displacement function in the radial direction

A remarkable characteristic of the SBFEM is that the solution is analytical in the radial direction. A radial nodal displacement function $\mathbf{u}(\xi)$ is introduced along the radial lines, where ξ varies from zero to one from the scaling centre to the boundary; the circumferential coordinates (η, ζ) are constant. The nodal displacement on the boundary can be expressed as $\{\mathbf{u}(\xi=1)\} = \mathbf{u}_b$, which can be obtained from the equilibrium equation. In addition, the directions of the displacement components are defined in the original Cartesian coordinates. A quadrangular isoparametric displacement model is used on the boundary to interpolate the displacement.

For 3D problems, the displacement components at a point (ξ, η, ζ) inside a pyramid are interpolated from the displacement function $\mathbf{u}(\xi)$, as shown in Eq. (2-12), where $[I]$ is a 3×3 identity matrix and $N_i (i=1,2,3,4)$ is the nodal interpolated function in an isoparametric element.

$$\mathbf{u}(\xi, \eta, \zeta) = \mathbf{N}^u(\eta, \zeta)\mathbf{u}(\xi) \quad (2-12a)$$

$$\mathbf{N}^u(\eta, \zeta) = [N_1[I], N_2[I], N_3[I], N_4[I]] \quad (2-12b)$$

$$\begin{aligned}
N_1 &= 0.25*(1 - \xi)(1 - \zeta) \\
N_2 &= 0.25*(1 + \xi)(1 - \zeta) \\
N_3 &= 0.25*(1 + \xi)(1 + \zeta) \\
N_4 &= 0.25*(1 - \xi)(1 + \zeta)
\end{aligned} \quad (2-12c)$$

Substituting Eqs. (2-12) and (2-10) into Eq. (2-2), the strains can be expressed as:

$$\boldsymbol{\varepsilon}(\xi, \eta, \zeta) = \mathbf{B}_1(\eta, \zeta)\mathbf{u}(\xi)_{,\xi} + \frac{1}{\xi}\mathbf{B}_2(\eta, \zeta)\mathbf{u}(\xi) \quad (2-13)$$

with the following two coefficient matrices:

$$\mathbf{B}_1(\eta, \zeta) = \mathbf{b}_1(\eta, \zeta)\mathbf{N}^u(\eta, \zeta) \quad (2-14a)$$

$$\mathbf{B}_2(\eta, \zeta) = \mathbf{b}_2(\eta, \zeta)\mathbf{N}^u(\eta, \zeta)_{,\eta} + \mathbf{b}_3(\eta, \zeta)\mathbf{N}^u(\eta, \zeta)_{,\zeta} \quad (2-14b)$$

2.4. Scaled boundary shape functions based on polyhedrons

The variational principle is introduced to derive the SBFEM equation in the nodal displacement function $\mathbf{u}(\xi)$. Simultaneously solving Eqs. (2-2), (2-4) and (2-5), the equilibrium equation can be expressed as:

$$E_0\xi^2\mathbf{u}(\xi)_{,\xi\xi} + (2E_0 + \mathbf{E}_1^T - \mathbf{E}_1)\xi\mathbf{u}(\xi)_{,\xi} + (\mathbf{E}_1^T - E_2)\mathbf{u}(\xi) + \mathbf{F}(\xi) = 0 \quad (2-15)$$

The coefficient matrices $\mathbf{E}_i(i=0,1,2)$ depend on only the geometry and the material properties of the domain, which are evaluated for the boundary surface elements and assembled over the discretized polyhedron boundary. In this paper, $\mathbf{F}(\xi)$ is a load vector that includes only the contributions from the body loads. Then, the equation can be rewritten as:

$$E_0\xi^2\mathbf{u}(\xi)_{,\xi\xi} + (2E_0 + \mathbf{E}_1^T - \mathbf{E}_1)\xi\mathbf{u}(\xi)_{,\xi} + (\mathbf{E}_1^T - E_2)\mathbf{u}(\xi) + \omega^2\mathbf{M}_0\xi^2\mathbf{u}(\xi) = 0 \quad (2-16)$$

with the following coefficient matrices and mass matrix:

$$E_0 = \int_{-1}^{+1} \int_{-1}^{+1} \mathbf{B}_1^T \mathbf{D} \mathbf{B}_1 |\mathbf{J}| d\eta d\zeta \quad (2-17a)$$

$$E_1 = \int_{-1}^{+1} \int_{-1}^{+1} \mathbf{B}_2^T \mathbf{D} \mathbf{B}_1 |\mathbf{J}| d\eta d\zeta \quad (2-17b)$$

$$E_2 = \int_{-1}^{+1} \int_{-1}^{+1} \mathbf{B}_2^T \mathbf{D} \mathbf{B}_2 |\mathbf{J}| d\eta d\zeta \quad (2-17c)$$

$$\mathbf{M}_0 = \int_{-1}^{+1} \int_{-1}^{+1} \rho \mathbf{N}^T \mathbf{N} |\mathbf{J}| d\eta d\zeta \quad (2-17d)$$

where \mathbf{B}_1 and \mathbf{B}_2 are the strain displacement transition matrices, \mathbf{D} is the constitutive matrix and \mathbf{N} is the shape function of a surface element.

Eq. (2-16) is a linear second-order ordinary differential equation (ODE) in matrix-form, where the analytical nodal displacement function $\mathbf{u}(\xi)$ can be derived in the radial direction. To solve the SBFEM equation, a variable $\mathbf{X}(\xi)$ that incorporates the nodal displacement function $\mathbf{u}(\xi)$ and the nodal force function $\mathbf{q}(\xi)$ is introduced:

$$\mathbf{X}(\xi) = \begin{Bmatrix} \xi^{0.5}\mathbf{u}(\xi) \\ \xi^{-0.5}\mathbf{q}(\xi) \end{Bmatrix} \quad (2-18)$$

This operation yields the first-order ODE:

$$\xi \mathbf{X}(\xi)_{,\xi} = -\mathbf{Z} \mathbf{X}(\xi) \quad (2-19)$$

where \mathbf{Z} is a Hamiltonian matrix, which is formulated using the coefficient matrices $\mathbf{E}_i(i=0,1,2)$ and the identity matrix \mathbf{I} :

$$\mathbf{Z} = \begin{bmatrix} E_0^{-1}\mathbf{E}_1^T - 0.5\mathbf{I} & -E_0^{-1} \\ -E_2 + \mathbf{E}_1\mathbf{E}_0^{-1}\mathbf{E}_1^T & -(E_1\mathbf{E}_0^{-1} - 0.5\mathbf{I}) \end{bmatrix} \quad (2-20)$$

Using eigenvalue decomposition, the matrix \mathbf{Z} can be decoupled

into pairs of eigenvalues λ_i and $-\lambda_i$, and the standard eigenvalue problem necessary for a polyhedron is formulated as:

$$\mathbf{Z} \begin{bmatrix} \boldsymbol{\psi}_u \\ \boldsymbol{\psi}_q \end{bmatrix} = \begin{bmatrix} \boldsymbol{\psi}_u \\ \boldsymbol{\psi}_q \end{bmatrix} \mathbf{S}_n \quad (2-21)$$

where \mathbf{S}_n is a diagonal matrix with entries that are composed of the real parts of the eigenvalues. The parameters $\boldsymbol{\psi}_u$ and $\boldsymbol{\psi}_q$ are the modal displacements and forces, respectively, and depend on the DOFs of the surface elements. For a bounded polyhedron, the solution to Eq. (2-16) can be formulated as:

$$\mathbf{u}(\xi) = \boldsymbol{\psi}_u \xi^{-(0.5+\mathbf{S}_n)} \mathbf{c} \quad (2-22a)$$

$$\mathbf{q}(\xi) = \boldsymbol{\psi}_q \xi^{0.5-\mathbf{S}_n} \mathbf{c} \quad (2-22b)$$

where the coefficient matrix \mathbf{c} is integration constants, which can be determined from the nodal displacement vector on the subdomain boundary $\mathbf{u}_b = \mathbf{u}(\xi=1)$:

$$\mathbf{c} = \boldsymbol{\psi}_u^{-1} \mathbf{u}_b \quad (2-23)$$

The general solutions for the displacements $\mathbf{u}(\xi)$ and nodal internal forces $\mathbf{q}(\xi)$ are obtained by substituting Eqs. (2-23) into Eq. (2-22):

$$\mathbf{u}(\xi) = \boldsymbol{\psi}_u \xi^{-\mathbf{S}_n} \boldsymbol{\psi}_u^{-1} \mathbf{u}_b \quad (2-24a)$$

$$\mathbf{q}(\xi) = \boldsymbol{\psi}_q \xi^{-\mathbf{S}_n} \boldsymbol{\psi}_u^{-1} \mathbf{u}_b \quad (2-24b)$$

Then, the displacement field $\mathbf{u}(\xi, \eta, \zeta)$ inside the polyhedral element is evaluated by substituting Eqs. (2-24a) into Eq. (2-12a) (see Fig. 1); this element can be expressed in terms of \mathbf{u}_b as:

$$\mathbf{u}(\xi, \eta, \zeta) = (\mathbf{N}^u(\eta, \zeta) \boldsymbol{\psi}_u \xi^{-(0.5+\mathbf{S}_n)} \boldsymbol{\psi}_u^{-1}) \mathbf{u}_b \quad (2-25)$$

Therefore, the polyhedron element shape functions $\boldsymbol{\Phi}(\xi, \eta, \zeta)$, similar to FEM, is extracted as:

$$\boldsymbol{\Phi}(\xi, \eta, \zeta) = \mathbf{N}^u(\eta, \zeta) \boldsymbol{\psi}_u \xi^{-(0.5+\mathbf{S}_n)} \boldsymbol{\psi}_u^{-1} \quad (2-26)$$

2.5. The strain and stress fields

The previous derivation provides the formulation for the nodal displacement function $\mathbf{u}(\xi)$. The strain field formulation proposed by Wolf [18] is expressed in Eq. (2-13), and the strain field of a polyhedron can be derived by substituting Eqs. (2-22a) into Eq. (2-13):

$$\begin{aligned}
\boldsymbol{\varepsilon}(\xi, \eta, \zeta) &= (\mathbf{B}^1(\eta, \zeta) \boldsymbol{\psi}_u (\mathbf{S}_n - 0.5) \xi^{-(1.5+\mathbf{S}_n)} \boldsymbol{\psi}_u^{-1}) \mathbf{u}_b \\
&\quad + \left(\frac{1}{\xi} \mathbf{B}^2(\eta, \zeta) \boldsymbol{\psi}_u \xi^{-(0.5+\mathbf{S}_n)} \boldsymbol{\psi}_u^{-1} \right) \mathbf{u}_b
\end{aligned} \quad (2-27)$$

Extracting the coefficient before \mathbf{u}_b , the strain fields of the scaled boundary finite element can be simplified as:

$$\boldsymbol{\varepsilon}(\xi, \eta, \zeta) = \mathbf{B}(\xi, \eta, \zeta) \mathbf{u}_b \quad (2-28a)$$

$$\begin{aligned}
\mathbf{B}(\xi, \eta, \zeta) &= (\mathbf{B}^1(\eta, \zeta) \boldsymbol{\psi}_u (\mathbf{S}_n - 0.5) \xi^{-(1.5+\mathbf{S}_n)} \boldsymbol{\psi}_u^{-1}) \\
&\quad + \left(\frac{1}{\xi} \mathbf{B}^2(\eta, \zeta) \boldsymbol{\psi}_u \xi^{-(0.5+\mathbf{S}_n)} \boldsymbol{\psi}_u^{-1} \right)
\end{aligned} \quad (2-28b)$$

where $\mathbf{B}(\xi, \eta, \zeta)$ is the strain-displacement matrix.

In elasto-plastic analysis, the incremental strain field can be decomposed into incremental elastic and plastic strain components. Then, the plastic strain increment can be determined from the plastic flow rule. Assuming associative plasticity and using the yield functions F and the plastic multiplier $\Delta\lambda$, the plastic strain increment is formulated as:

$$\begin{aligned}
\Delta\boldsymbol{\varepsilon} &= \Delta\boldsymbol{\varepsilon}_e + \Delta\boldsymbol{\varepsilon}_p \\
\Delta\boldsymbol{\varepsilon}_p &= \frac{\partial F}{\partial \boldsymbol{\sigma}} \Delta\lambda
\end{aligned} \quad (2-29)$$

where $F=F(\boldsymbol{\sigma}, \kappa)$ is defined as the yield function in the formulation and

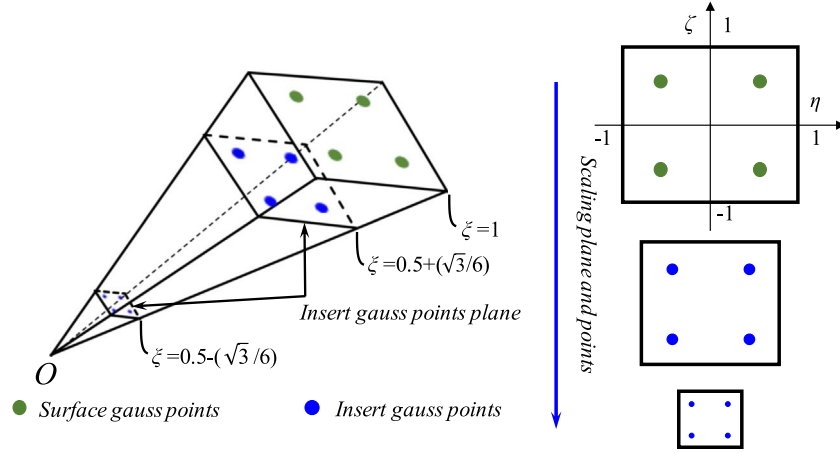


Fig. 3. The distribution and location of the Gauss points in a pyramid.

is determined from the current stress state σ and the hardening parameter κ . Using Hooke's law, the incremental stress field $\Delta\sigma$ can be written as:

$$\Delta\sigma = D_{ep}\Delta\epsilon \quad (2-30)$$

where D_{ep} is the elasto-plastic constitutive matrix. Substituting Eq. (2-28) into the formulation for the incremental strain field $\Delta\epsilon$, the incremental stress field is expressed as:

$$\Delta\sigma(\xi, \eta, \zeta) = D_{ep}B(\xi, \eta, \zeta)\Delta u_b \quad (2-31)$$

where Δu_b is the nodal displacement increment on the boundary surface.

3. Polyhedron formulation for elasto-plastic analysis

The previous section presents the necessary equations for the remaining introduction. The elasto-plastic formulation of polyhedral elements based on the SBFEM is derived in this section. Once the nodal displacements are solved using the previously presented derivation, the displacement field over the discretized subdomain can easily be interpolated. Similar to FEM, the scaled boundary polyhedron formulation for elasto-plasticity is derived using the principle of virtual work, which is written in SBFEM coordinates as:

$$\int_{\Omega} \delta \epsilon^T \Delta \sigma(\xi, \eta, \zeta) d\Omega = \int_{\Gamma} \delta u^T f_t d\Gamma + \int_{\Gamma} \delta u^T f_b d\Gamma - \int_{\Omega} \delta \epsilon^T \sigma(\xi, \eta, \zeta) d\Omega \quad (3-1)$$

where $\Delta\sigma(\xi, \eta, \zeta)$ is the incremental stress field, f_t and f_b are the surface traction and body force intensity, respectively, and $\delta\epsilon(\xi, \eta, \zeta)$ is the virtual strain field corresponding to the virtual displacement field $\delta u(\xi, \eta, \zeta)$. Substituting the equations for these variables from the previous sections, the expanded formulation of Eq. (3-1) can be expressed as:

$$\begin{aligned} & \left(\int_{\Omega} B^T(\xi, \eta, \zeta) D_{ep} B(\xi, \eta, \zeta) d\Omega \right) \Delta u_b \\ &= \left(\int_{\Gamma} \Phi^T(\xi, \eta, \zeta) f_t d\Gamma + \int_{\Gamma} \Phi^T(\xi, \eta, \zeta) f_b d\Gamma \right) \\ & \quad - \left(\int_{\Omega} B^T(\xi, \eta, \zeta) \sigma(\xi, \eta, \zeta) d\Omega \right) \end{aligned} \quad (3-2)$$

where D_{ep} is the elasto-plastic constitutive matrix calculated from the constitutive model. In addition, the term within the first set of parentheses on the left-hand side of Eq. (3-2) is the elasto-plastic stiffness matrix of the polyhedron K_{ep} ; the term within the second set of parentheses is the external load vector R_{ext} ; and the term within the third set of parentheses is the internal load vector R_{int} . Thus, Eq. (3-2) can be simplified as:

$$K_{ep} \Delta u_b = R_{ext} - R_{int} \quad (3-3)$$

Similar to FEM, Eq. (3-3) is a system of nonlinear equilibrium equations, which can be assembled polyhedron-by-polyhedron. Then, the total equilibrium equation of the discretized domain is described as:

$$\left(\sum_{i=1}^{nPol} K_{ep} \right) \Delta U_b = \sum_{i=1}^{nPol} (R_{ext} - R_{int}) \quad (3-4)$$

where ΔU_b is the incremental nodal displacement vector on the boundary of the whole domain. Standard nonlinear iterative procedures such as the modified Newton-Raphson iterations can be used to solve this equation.

3.1. Calculation of the elasto-plastic stiffness matrix

Since the SBFEM is semi-analytical and discretizes only on the boundary, the Gauss integration points are only on the boundary surface. These Gauss points cannot describe the nonlinear characteristics inside the elements, which severely limits the application of SBFEM in nonlinear fields. To overcome this limitation and to broaden the range of applications, this study presents a novel approach.

The quadrilateral isoparametric element is employed on the boundary, as shown in Fig. 2(b). In addition, four Gauss points are selected to calculate the SBFEM coefficient matrices on the discrete boundary. The coordinate ξ varies from zero to one from the scaling centre to the boundary surface in the radial direction. According to the principle of Gauss integration and by scaling the boundary surface Gauss points, the distribution applied to the integration points is illustrated in Fig. 3; the values of the points located at $0.5 \times (1 \pm \frac{\sqrt{3}}{3})$ are considered.

A polyhedron formulation of the elasto-plastic stiffness matrix can be derived from Eq. (3-2) and Eq. (3-3), as shown in Eq. (3-5).

$$K_{ep} = \int_{\Omega} B^T(\xi, \eta, \zeta) D_{ep} B(\xi, \eta, \zeta) d\Omega \quad (3-5)$$

Then, the K_{ep} of the polyhedron is determined by integrating over each discretized pyramid with the corresponding Gauss points in the ξ -direction.

$$K_{ep} = \sum_{i=1}^{8m} B^i(\xi, \eta, \zeta) D_{ep}^i B^i(\xi, \eta, \zeta) V_i \quad (3-6)$$

where $B^i(\xi, \eta, \zeta)$ denotes the strain displacement transformation matrix determined by the i^{th} Gauss point, which can be obtained from Eqs. (2-24); D_{ep} represents the elasto-plastic constitutive matrix of the i^{th} Gaussian and is calculated from the corresponding plasticity model; and V_i is the volume of the i^{th} point in the V_e . The total elasto-

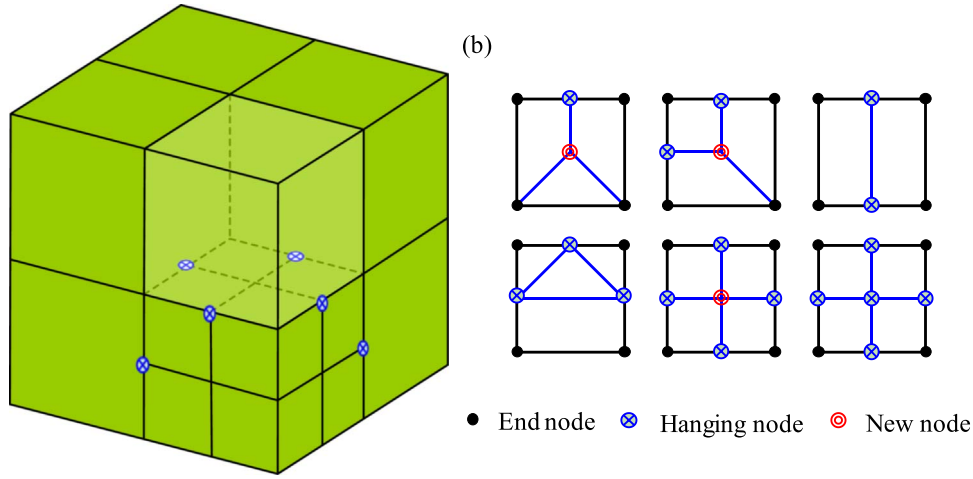


Fig. 4. Representative octree meshing for the possible hanging node configurations on each face: (a) Balanced octree mesh (b) Possible hanging node configurations on each face.

plastic stiffness matrix of the discretized domain can be evaluated after each \mathbf{K}_{ep} has been determined for the polyhedrons.

3.2. Calculation of the external load vector

The external load vector \mathbf{R}_{ext} can be extracted from Eq. (3-2) and is expressed as

$$\mathbf{R}_{ext} = \int_{\Gamma} \Phi^T(\xi, \eta, \zeta) f_i d\Gamma + \int_{\Omega} \Phi^T(\xi, \eta, \zeta) f_b d\Omega \quad (3-7)$$

The first term on the right-hand side of Eq. (3-7) is the distributed load on the boundary. It can be further simplified by considering that $(\xi=1) \Phi(\xi, \eta, \zeta) = \mathbf{N}^u(\eta, \zeta)$ applies at the polyhedron boundary; this can be written as:

$$\int_{\Gamma} \Phi^T(\xi, \eta, \zeta) f_i d\Gamma = \int_{-1}^1 \mathbf{N}^u(\eta, \zeta) [\mathbf{J}(\eta, \zeta)]^T f_i d\eta d\zeta \quad (3-8)$$

The second term is the body load vector. For the case of a constant body load, this term is expressed by combining it with Eqs. (2-23) and numerically integrating with the Gauss points:

$$\int_{\Omega} \Phi^T(\xi, \eta, \zeta) f_b d\Omega = \sum_{k=1}^m \sum_{i=1}^8 [\mathbf{N}_{ki}^u(\eta, \zeta) \psi_u \xi_i^{-(0.5+S_n)} \psi_u^{-1}]^T f_b V_{ki} \quad (3-9)$$

where m represents the number of surface elements in a polyhedron, k denotes the k th surface element and i denotes the i th Gauss point in a pyramid.

3.3. Calculation of the internal load vector

The formulation of the load vector that results from the internal stresses is defined in Eq. (3-10), which is determined from Eq. (3-2).

$$\mathbf{R}_{int} = \int_{\Omega} \mathbf{B}^T(\xi, \eta, \zeta) \boldsymbol{\sigma}(\xi, \eta, \zeta) d\Omega \quad (3-10)$$

Here, the numerical integration is introduced into the evaluation. First, the strain field $\boldsymbol{\epsilon}(\xi, \eta, \zeta)$ can be calculated from Eqs. (2-24) after determining the nodal displacements \mathbf{u}_b on the boundary of the domain. Then, the stress field $\boldsymbol{\sigma}_i(\xi, \eta, \zeta)$ on each Gauss point is determined by substituting the elasto-plastic constitutive matrix \mathbf{D}_{iep} , and the formulation is expressed as:

$$\mathbf{R}_{int} = \sum_{k=1}^n \sum_{i=1}^8 \mathbf{B}^{ki}(\xi, \eta, \zeta)^T \boldsymbol{\sigma}_{ki}(\xi, \eta, \zeta) V_{ki} \quad (3-11)$$

4. Scaled boundary polyhedron procedure for elasto-plasticity

The polyhedral element of the SBFEM, PSBFEM_Volume (integrated over the volume) was implemented using object-oriented programming in Visual C++, based on the Windows programs GEODYNA [19], which was developed by the second author. Multi-core parallel technology is used in the GEODYNA program to provide the computational ability to solve large-scale elasto-plastic analysis problems that include millions of DOFs.

5. Octree mesh methodology

The octree is a hierarchical tree-like data structure that is used to describe a 3D space. This technique can be considered a 3D extension of the quad-tree; in the octree, each node represents the volume of a cube. Further descriptions can be found in references [5,6].

A subdomain possesses six square faces. The standard shape function of a quadrangular isoparametric element is used in this paper, so each surface should be meshed into a quadrangle or triangle. To improve the efficiency in a fine analysis, only some subdomains are subdivided, which generates hanging nodes. Consequently, where the isoparametric element cannot be used, the sides of the surface element are changed. Hence, the boundary surfaces with hanging nodes need to be addressed. Some new nodes are introduced to accomplish this purpose, and the subdomains are divided into a combination of triangular and quadrilateral elements by connecting the new nodes and the hanging nodes. The six possible categories are shown in Fig. 4(b).

Due to the limited number of patterns in the octree decomposition, the stiffness and mass matrices of these cubic octants can be pre-computed and stored for quick retrieval. The stiffness and mass matrices of two similar cubic octants with different sizes are simply scalar multiples.

6. Numerical example

This section describes numerical simulations that are used to validate the nonlinear polyhedron SBFEM. The numerical algorithm discussed in the previous section was implemented in the finite element program GEODYNA. This section is divided into two subsections: single-element experimental tests that verify the validity of the numerical integration of NPSBFEM3D and a structural application.

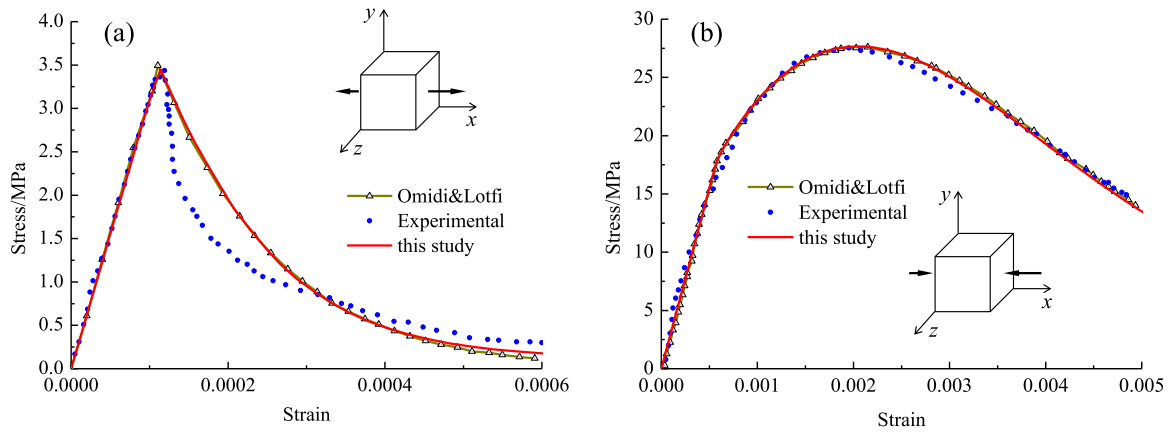


Fig. 5. Monotonic uniaxial loading compared with experimental [20,21] and numerical results from the literature [22,23]; (a) Tension (b) Compression.

6.1. Procedure verification

Experimental tests [20,21] were conducted using a single 8-node plane stress element, and the loads were applied using displacement control. A plastic damage [23] model was used, and the following material properties were used for all the cases: elastic modulus, $E=31.0$ GPa (tensile) and 31.7 GPa (compressive); Poisson's ratio $\nu=0.18$; density $\rho=2400$ kg/m³; compressive strength $f_{c0}=27.6$ MPa; tensile strength $f_{t0}=3.48$ MPa; fracture energy $G_c=1750$ N/m (compressive) and $G_t=12.3$ N/m (tensile); $l_c=25.4$ mm; and $\alpha_p=0.2$ [22].

6.1.1. Monotonic uniaxial loading

The performance of the studied element was validated through previous uniaxial tensile and compressive loading experiments. The results were compared with the corresponding experiments [20,21] and numerical results from the literature [22,23], as illustrated in Fig. 5a and b. This figure shows that the numerical simulations correspond well with the previous experimental and numerical results for uniaxial tensile and compressive loading.

6.2. Notched concrete beam under four-point bending

The simulation of a notched concrete beam monotonically loaded under four-point bending is investigated to evaluate the performance of the presented method in a 3-D structural application. Many studies can be found in both experiments and numerical modelling. The specifications of the simulation are illustrated in Fig. 6(a), and the corresponding grid is also shown in Fig. 6(b), where the hexahedron and polyhedron elements are used.

The material properties are listed in Table 1, and the calculation is carried out under the applied displacement controlled.

Fig. 7 demonstrates the load P versus the load point deflection for the numerical simulation and the corresponding experimental test and the findings from literature [22]. The results excellently agree with one another, which confirm the validity of the method. The damage development at the end of the simulation is also illustrated in Fig. 8, which is clearly showing the localization in the model.

6.3. Verification example for seismic damage of a concrete gravity dam

To investigate the applicability of the NPSBFEM3D for simulating elasto-plastic seismic problems, the dynamic response of Koyna concrete dam [24] was simulated. This dam was damaged during a strong earthquake, which is treated as a classical research object.

6.3.1. Modelling

The dam studied in this paper is 850 m long; as shown in Fig. 9(a),

a typical non-overflow monolith with a thickness of 2 m was selected for 3D seismic analysis using the proposed NPSBFEM3D. This overflow monolith is 103 m high with a reservoir depth of 91.7 at the time of the earthquake [25]. The finite element mesh of the dam is shown in Fig. 9(b). The mesh in region 1 was refined for a more detailed simulation of the damage region. To remedy the cross-scale between regions 1 and 2, polyhedral elements evolved from the octree mesh were used.

Additionally, in order to evaluate the integration method for the triangular elements as well, a similar study was conducted considering the boundary of a subdomain was also divided into triangular, which lead to a total of 9625 elements, 9990 nodes and 29,970 DOFs.

The cross-scale mesh was introduced to decrease the number of elements, as illustrated in Fig. 10. The hanging nodes were handled with two configurations on the corresponding face, which lead to a total of 3901 elements, 8278 nodes and 24,834 DOFs.

6.3.2. Parameter identification

A plastic damage model [23] was used to simulate the failure modes of the concrete dam. According to the available literature [26], the following properties were used in the analysis: a density ρ of 2630 kg/m³, a modulus of elasticity E of 31 GPa, a Poisson's ratio ν of 0.2, a tensile strength of 2.90 MPa, and a fracture energy of 250 N m. The dam was subjected to its self-weight and to hydrostatic pressure prior to any earthquake excitation. The foundation was considered rigid, and the dynamic water pressure was considered according to the added mass method [27].

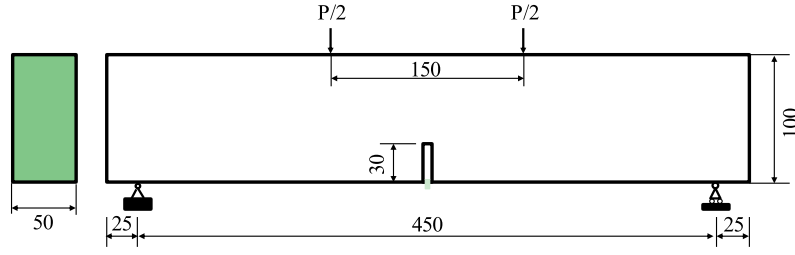
As the compressive strength of concrete is considerably higher than its tensile strength, only the tensile damage of Koyna concrete dam was considered in this study.

6.3.3. Input ground motions

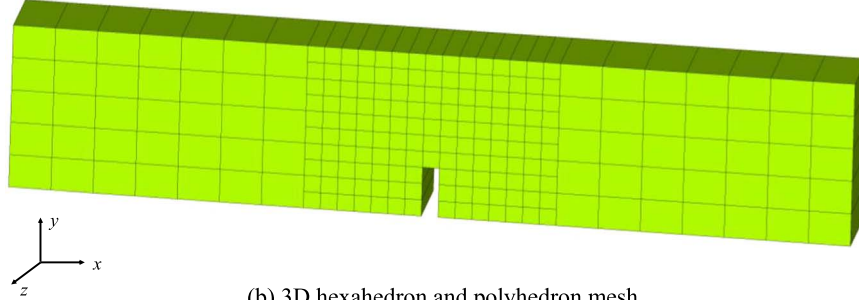
An earthquake with a magnitude of 6.5 on the Richter scale occurred near Koyna concrete dam on December 11, 1967, with a maximum acceleration measured at the foundation gallery of $0.49g$ and $0.34g$ in the horizontal and vertical directions, respectively. This earthquake caused very serious structural damage to the dam, including horizontal cracks on the upstream and downstream faces of a number of non-overflow monoliths near the elevation where the slope of the downstream face changes abruptly. The Koyna acceleration records during the seismic wave in 1967 is shown in Fig. 11; these were used as the input motions in the upstream-downstream and vertical directions with a time step of 0.005 s.

6.3.4. Damping

The damping matrix was formulated using the assemblage of element-damping matrices as shown in Eq. (6-1), and each element satisfied Eq. (6-2) according to Rayleigh damping:



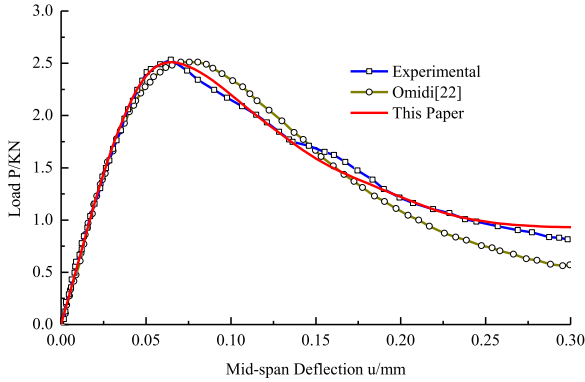
(a) geometry of the notched beam and boundary conditions (unit: mm)



(b) 3D hexahedron and polyhedron mesh

Fig. 6. Notched concrete beam for four-point bending test.**Table 1**
Material properties for the notched concrete beam.

E_0 (GPa)	ν	f_t (MPa)	f_c (MPa)	G_t (N/m)	G_c (N/m)
38.0	0.2	2.9	30.0	65.0	6500

**Fig. 7.** Load-deflection curves for the simulation and compared with the experiment result, finding from literature.

$$[C]_e = \alpha_e [M]_e + \beta_e [K]_e \quad (6-1)$$

$$\lambda_e = \frac{1}{2} \left(\frac{\alpha_e}{\omega} + \beta_e \omega \right) \quad (6-2)$$

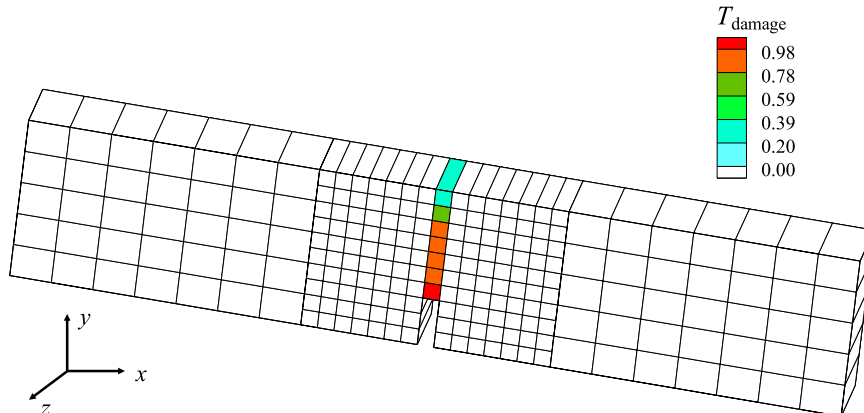
where $\omega = 2\pi f$ is the circular frequency. Martin et al. [28] proposed a method for determining the values of α_e and β_e based on the predominant frequencies of the structure and the input motion; this method was employed in this study:

$$\begin{cases} \alpha_e = 2\lambda_e \frac{\omega_1 \omega_2}{\omega_1 + \omega_2} \\ \beta_e = 2\lambda_e \frac{1}{\omega_1 + \omega_2} \\ \omega_2 = n\omega_1 \end{cases} \quad (6-3)$$

where ω_1 and ω_2 are the dominant circular frequencies of the structure and input motion, respectively. In this study, the damping ratio for the concrete was assumed to be 5% in the dynamic analysis [29].

6.4. Results and discussion

Four significant moments of the plastic damage in Koyna dam under the seismic wave are presented in Fig. 12, where T_{damage} represents the tensile damage factor that varies from zero to one. Due to the infinite rigidity of the foundation, the stress concentration

**Fig. 8.** Tensile damage at the end of the simulation.

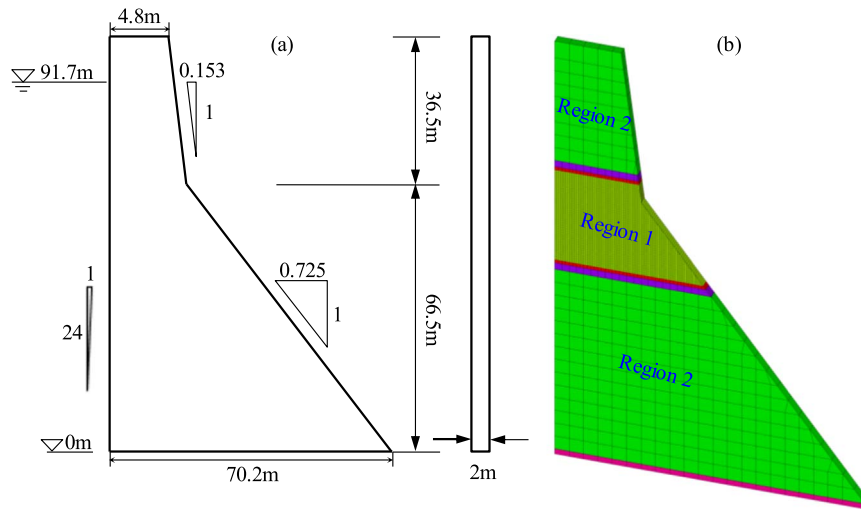


Fig. 9. Geometry and mesh of Koyuna concrete dam.

induces the first damage zone propagation in the concrete, in which a distinct damage zone is initiated at the base of the dam at 3.200 s. Thereafter, the compressive stresses resulting from the rocking of the top block causes several elements on the upstream face to soften and localized damage to appear. The second damage area in the concrete originates at 4.000 s on the downstream face along with the propagating of the first damage zone, as shown in Fig. 12(b). When the load is reversed, a straight damage zone is then developed that curves down at 4.700 s, as shown in Fig. 12(c). The damage strip traced to the downstream area is translated into horizontal damage at 6.250 s.

The processing of the global damage zone at four selected times is presented. In this study, experimental shaking table test results [30] and the findings of other researchers are introduced to verify the reliability of NPSBFEM3D. The global damage zone with mesh is shown in Fig. 13(a), which clearly presents the plastic damage distribution. The damage zone is concentrated, and the dam retains its overall stability because the upstream and downstream faces are not under tensile stress at the same time. In addition, the damage profiles

agree with the results of previous studies on the same dam [23,25].

The tensile damage gradually developed during the earthquake; if T_{damage} exceeded 0.8 in certain elements, cracking occurred in the concrete [23]. This rule is taken as a criterion for considering the elements connected to those where T_{damage} exceeded 0.8 as an interconnected crack. Experimental shaking table test results [30], an extended finite element method (XFEM) simulation of the crack propagation [31] and other findings from the literature were used to verify the validity of NPSBFEM3D. In addition, Fig. 14 compares the predicted global crack profile. The potential failure modes for the different methods are basically the same. The NPSBFEM3D procedure satisfactorily predicted the damage zone profiles and the development process, thus indicating that it is reasonable to conduct elasto-plastic analysis using SBFEM.

Obviously, the results are reasonable as well using the triangular elements, and the global development of damage zone illustrated in Fig. 13(b) is basically the same, which demonstrates the integration method is applicative for triangle elements.

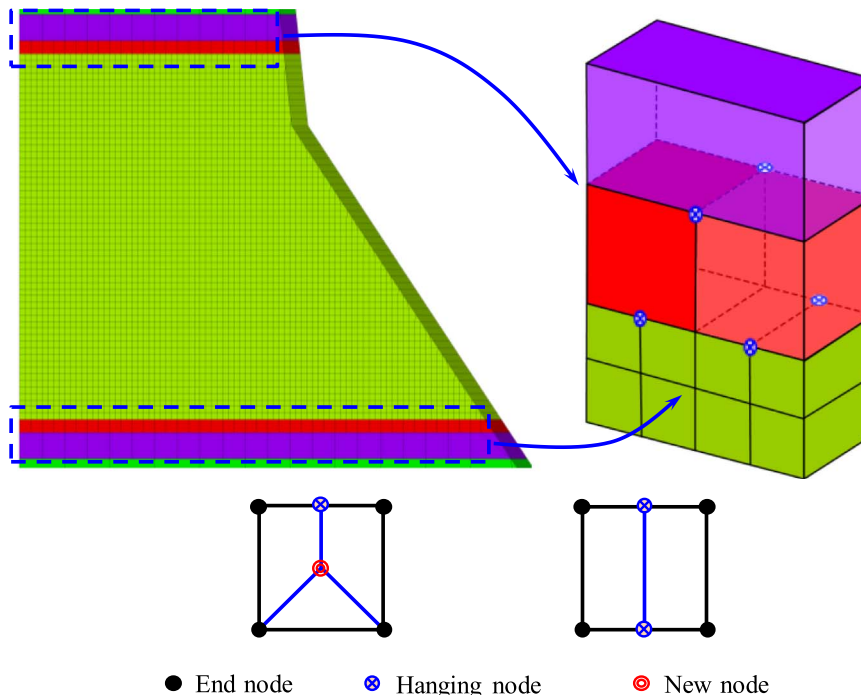


Fig. 10. Detail of the cross-scale mesh.

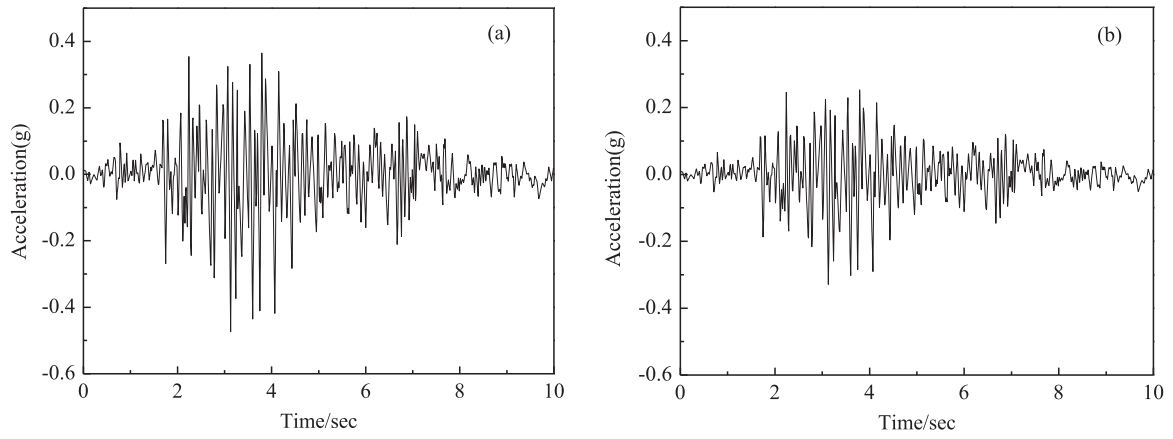


Fig. 11. Koyna acceleration records: (a) Downstream flow (b) Vertical flow.

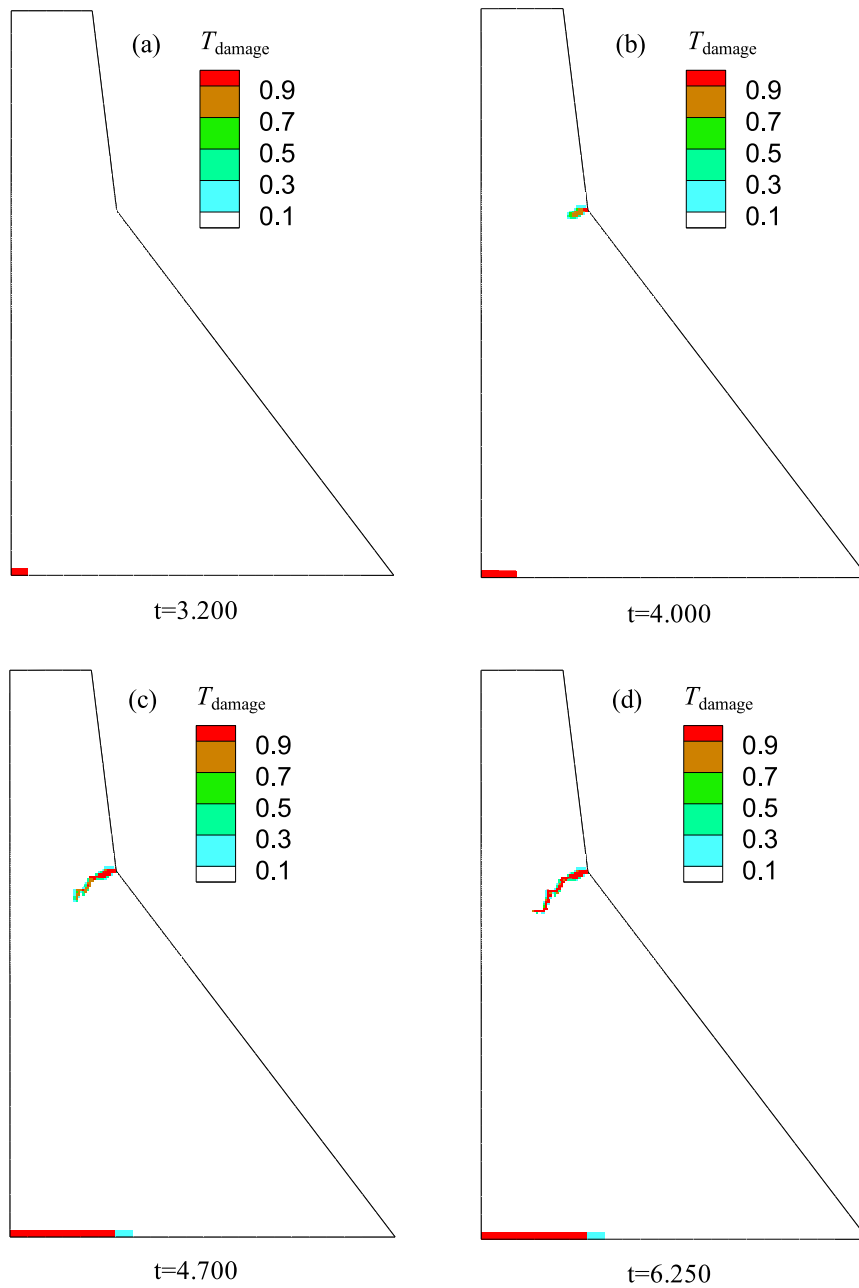


Fig. 12. The evolution of cumulative tensile damage in Koyna dam.

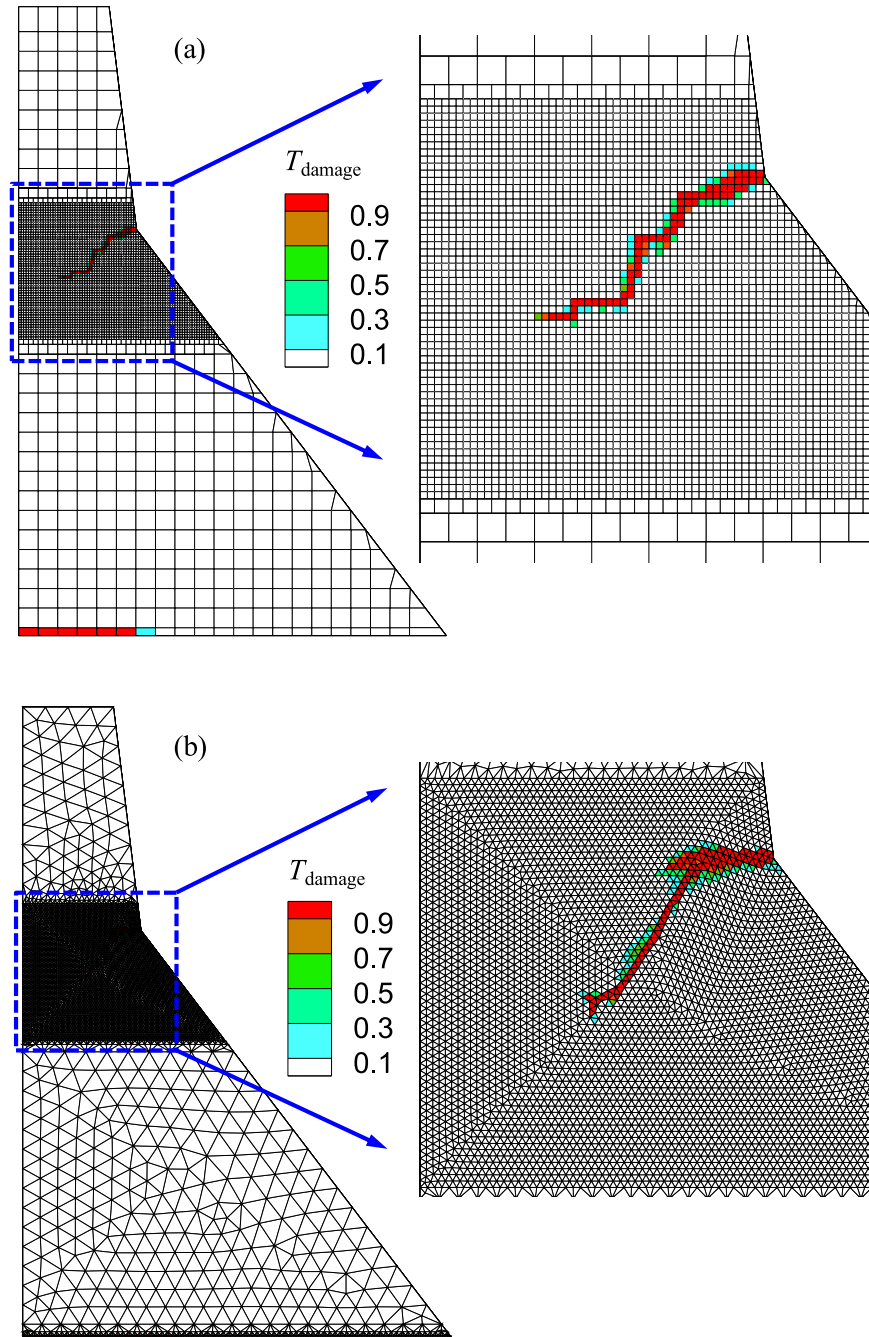


Fig. 13. Final distribution of the global damage with mesh in Koyna dam: (a) the boundary of a subdomain is quadrilateral elements, and (b) the boundary of a subdomain is triangular elements.

7. Conclusions

This paper proposed a nonlinear approach for NPSBFEM3D, which permits an arbitrary number of faces in the polyhedron element. Referring to the Gauss quadrature rules in the conventional FEM, four Gauss points were introduced in the plane where the coordinate ξ is equal to $0.5 \times (1 \pm \frac{\sqrt{3}}{3})$ in the radial direction. The element shape function was constructed using the semi-analytical solution derived from elastic surface elements, and integration was conducted with the adopted Gauss points for nonlinear analysis. Eventually, elasto-plastic analysis can be performed using SBFEM as conveniently as when using FEM.

To verify the validity and reliability of the NPSBFEM3D, an experimental test with uniaxial tensile and compressive loading was

simulated; the proposed method performed as well as the approaches from the literature. In addition, the classical research verification example of the Koyna concrete dam was presented. A plastic damage model was used to simulated the seismic damage of the gravity dam. Then, the simulation results were compared with the experimental results and the findings from other studies, which showed strong agreement.

The SBFEM has been extensively employed in linear structure problems since it was presented. However, the application of this method is very rare in nonlinear fields, which greatly restricts its applications. In this paper, the method is extended to the fields of research and industry as a versatile and promising procedure for elasto-plastic analysis. The presented method inherits the advantages of FEM, BEM and polyhedrons, allowing it to conduct nonlinear

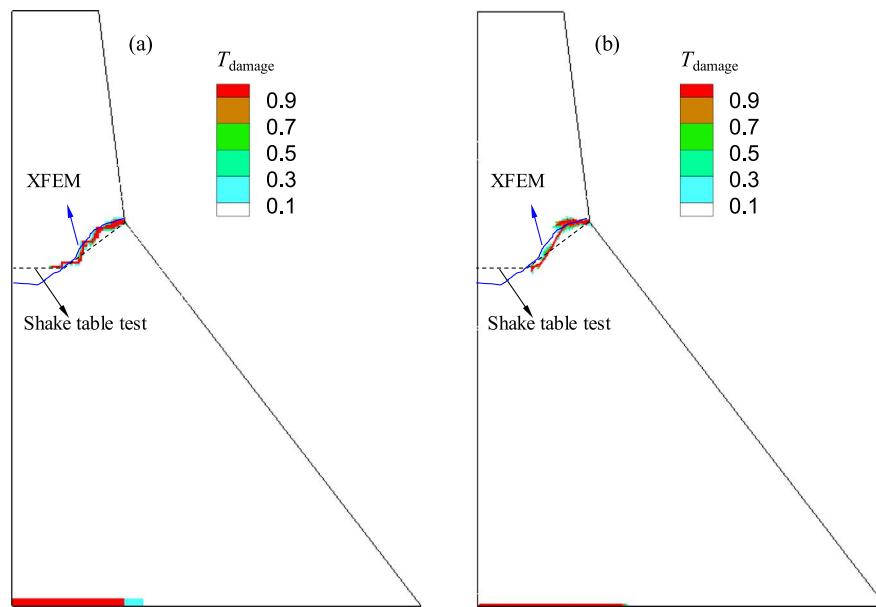


Fig. 14. Comparison of the simulation results and the shaking table test results: (a) the boundary of a subdomain is quadrilateral elements, and (b) the boundary of a subdomain is triangular elements.

numerical simulations of elaborate and cross-scale engineering structures.

The focus of this study was demonstrating the applicability of the presented polyhedral SBFEM for solving elasto-plastic problems. Some exploratory topics could be investigated in the future to make this method more convenient, efficient and versatile. For instance, the face elements are considered to be either triangles or quadrangles, and the quadrangular isoparametric element shape function is used in a polyhedron. Constructing a polygon shape function for a polygonal surface boundary element would be a further extension of this study. This method will become more universal if the confirming shape function of the polygonal boundary surface element is constructed.

Acknowledgements

This work was supported by the National Natural Science Foundation of China (Grant No. 51379028, 51421064, 51279025). This financial support is gratefully acknowledged.

References

- [1] Song C, Wolf JP. The scaled boundary finite-element method—alias consistent infinitesimal finite-element cell method—for elastodynamics. *Comput Methods Appl Mech Eng* 1997;147(3):329–55.
- [2] Wolf JP, Song CM. *Finite-element modelling of unbounded media*. Chichester: Wiley; 1996.
- [3] Goswami S, Becker W. Computation of 3-D stress singularities for multiple cracks and crack intersections by the scaled boundary finite element method. *Int J Fract* 2012;175(1):13–25.
- [4] Hell S, Becker W. The scaled boundary finite element method for the analysis of 3D crack intersection. *J Comput Sci* 2015;9:76–81.
- [5] Saputra AA, Birk C, Song C. Computation of three-dimensional fracture parameters at interface cracks and notches by the scaled boundary finite element method. *Eng Fract Mech* 2015;148:213–42.
- [6] Saputra AA, Ooi ET, Birk C. et al. Three-dimensional transient fracture analysis using scaled boundary finite elements and octree mesh; 2014.
- [7] Man H, Song C, Gao W, et al. A unified 3D-based technique for plate bending analysis using scaled boundary finite element method. *Int J Numer Methods Eng* 2012;91(5):491–515.
- [8] Liu J, Zhang P, Lin G, et al. Solutions for the magneto-electro-elastic plate using the scaled boundary finite element method. *Eng Anal Bound Elem* 2016;68:103–14.
- [9] Gravenkamp H, Man H, Song C, et al. The computation of dispersion relations for three-dimensional elastic waveguides using the scaled boundary finite element method. *J Sound Vib* 2013;332(15):3756–71.
- [10] Birk C, Behnke R. A modified scaled boundary finite element method for three-dimensional dynamic soil-structure interaction in layered soil. *Int J Numer Methods Eng* 2012;89(3):371–402.
- [11] Yang ZJ, Wang XF, Yin DS, et al. A non-matching finite element-scaled boundary finite element coupled method for linear elastic crack propagation modelling. *Comput Struct* 2015;153:126–36.
- [12] Huang YJ, Yang ZJ, Liu GH, et al. An efficient FE-SBFE coupled method for mesoscale cohesive fracture modelling of concrete. *Comput Mech* 2016:1–21.
- [13] Luo T, Ooi ET, Chan AHC. et al. A coupled scaled boundary-discrete-finite element method for particle breakage modelling in granular media. In: 12th world congress on computational mechanics and 6th asia-pacific congress on computational Mechanics; 2016.
- [14] Lin Zhi, Liao liang, et al. The scaled boundary FEM for nonlinear problems. *Commun Nonlinear Sci Numer Simul* 2011;16(1):63–75.
- [15] Ooi ET, Song C, Tin-Loi F. A scaled boundary polygon formulation for elasto-plastic analyses. *Comput Methods Appl Mech Eng* 2014;268:905–37.
- [16] Liao S. An optimal homotopy-analysis approach for strongly nonlinear differential equations. *Commun Nonlinear Sci Numer Simul* 2010;15(8):2003–16.
- [17] Bransch M, Lehmann L. A nonlinear HHT- α method with elastic-plastic soil-structure interaction in a coupled SBFEM/FEM approach. *Comput Geotech* 2011;38(1):80–7.
- [18] Wolf JP, Schanz M. *The scaled boundary finite-element method*. Chichester, U.K: Wiley; 2004.
- [19] Degao Z, Xianjing K, Bin X. User manual for geotechnical dynamic nonlinear analysis. Dalian: Institute of Earthquake Engineering, Dalian University of Technology; 2005.
- [20] Gopalratnam VS, Shah SP. Softening response of plain concrete in direct tension. *Acids J* 1985;3:310–23.
- [21] Karsan ID, Jirsa JO. Behavior of concrete under compressive loading. *J Struct Div ASCE* 1969;95(12):2535–63.
- [22] Omid O, Lotfi V. Finite element analysis of concrete structures using plastic damage model in 3-D implementation. *Int J Civ Eng* 2010;8(3):187–203.
- [23] Lee J, Fenves GL. A plastic-damage model for cyclic loading of concrete structures. *J Eng Mech ASCE* 1998;124:892–900.
- [24] Chopra AK, Chakrabarti P. The Koyna earthquake and the damage to Koyna dam. *Bull Seismol Soc Am* 1973;63(2):381–97.
- [25] Pan J, Zhang C, Xu Y, et al. A comparative study of the different procedures for seismic cracking analysis of concrete dams. *Soil Dyn Earthq Eng* 2011;31(11):1594–606.
- [26] Wang C, Zhang S, Sun B, et al. Methodology for estimating probability of dynamical system's failure for concrete gravity dam. *J Cent South Univ* 2014;21:775–89.
- [27] Xu H, Zou D, Kong X, et al. Study on the effects of hydrodynamic pressure on the dynamic stresses in slabs of high CFRD based on the scaled boundary finite-element method. *Soil Dyn Earthq Eng* 2016;88:223–36.
- [28] Martin Hudson, Idriss IM, Mohsen Beiken. User manual for Quad4m: a computer program to evaluate the seismic response of soil structures using finite element procedures and incorporating a compliant base. California: University of California; 1994.
- [29] Xu B, Zou D, Kong X, et al. Dynamic damage evaluation on the slabs of the concrete faced rockfill dam with the plastic-damage model. *Comput Geotech* 2015;65:258–65.
- [30] Hall JF. The dynamic and earthquake behaviour of concrete dams: review of experimental behaviour and observational evidence. *Soil Dyn Earthq Eng* 1988;7(2):56–121.
- [31] Zhang S, Wang G, Yu X. Seismic cracking analysis of concrete gravity dams with initial cracks using the extended finite element method. *Eng Struct* 2013;56:528–43.